Paramagnetic defects in $BaTiO_3$ and their role in light-induced charge transport. I. ESR studies

1992 J. Phys.: Condens. Matter 4 4719

(http://iopscience.iop.org/0953-8984/4/19/013)

J. Phys.: Condens. Matter 4 (1992) 4719–4742. Printed in the UK

Paramagnetic defects in $BaTiO_3$ and their role in light-induced charge transport: I. ESR studies

E Possenriede, P Jacobs and O F Schirmer

Fachbereich Physik, Universität Osnabrück, D-4500 Osnabrück, Federal Republic of Germany

Received 23 December 1991

Abstract. An overview on paramagnetic defects in $BaTiO_3$ single crystals, used in photorefractive applications, is given. New results concerning cation defects include the investigation of double quantum transitions in isolated Fe^{3+}, identification of the parameters of Fe^{4+}–V_O, analysis of Co^{2+}, the report of Co^{4+}–V_O, Jahn–Teller-induced spin–lattice relaxation effects of Pt^{3+}, identification of Rh^{2+}, Rh^{4+}, Ir^{4+} and Pt^{5+}. In the field of anion defects O^- trapped hole centres associated with unknown acceptors and with Al^{3+} are reported. The role of the identified defects in light-induced charge transport processes is discussed.

1. Introduction

The promising photorefractive properties of $BaTiO_3$ [1], triggered by photoionization of suitable defects, have revived the interest in the study of paramagnetic lattice perturbations in this material. Knowledge of the specific features of possible defects in a photorefractive compound is necessary in order to optimize the performance of the material, such as speed and maximum refractive index changes. Where applicable, electron spin resonance is able to furnish rather detailed information on the chemical and electronic structure of paramagnetic defects. We therefore have begun a systematic ESR study of such lattice perturbations in $BaTiO_3$. A report on the presently available results will be given here. This investigation will be the basis for the elucidation of the light-induced charge transport processes in which the defects identified here are involved; these can possibly be responsible for the photorefractive index changes. The connection between these light-dependent features of the defects and their structural properties will be dealt with in a second paper, hereafter called II.

In this second report, the investigations will be based on the dependence of the ESR intensities on the wavelengths of light illumination. In most cases the photostimulated charge transport paths, initiating the photorefractive effect, can be identified in this way. By simultaneously monitoring the changes of ESR and optical density under illumination, a correlation between the structural and optical properties will be established in some instances. Our aim is to extend, by consistency arguments, the information obtained from the optical absorption of centres known from ESR to those cases, where the defects are ESR silent, and to arrive then at an overall picture of possible defects in $BaTiO_3$.

0953-8984/92/194719+24$04.50

A principal problem concerning the role of defects in the photoconductivity of $BaTiO_3$ has been solved recently. It was shown [2–4] that two types of levels are needed to explain, e.g., the sublinear dependence of photoconductivity on light intensity, $\sigma_{ph} \propto I^x$, $x \leqslant 1$. One of the centres responsible for these levels is deep with respect to the neighbouring bands in the sense that thermal ionization can be neglected as compared to photoionization. The other type of centres is shallow; they can intermediately trap the quasifree charge carriers. Competition between light-induced and thermal ionization of these traps then leads to $x < 1$ [3]. The transfer of charges between deep and shallow levels also causes photochromic changes in the optical absorption of the material.

It is our central goal to identify the defects causing these two types of levels in the various crystals investigated. In several cases the experiments were performed on crystal specimens which had been characterized by other authors [5] with respect to the wavelength dependence of carrier sign and photoconductivity. It will be shown that in nominally pure or Fe-doped material the hole ionization level of Fe^{4+}, designated $Fe^{4+/3+}$, is the most effective deep one, if these specimens are used as-grown or oxidized. In Co-doped crystals the corresponding deep level is $Co^{3+/2+}$. The shallow levels in some cases are derived from O^- centres, corresponding to holes which have been captured at O^{--} near unidentified acceptor defects. In most cases, however, we have found that shallow levels are connected with defects which apparently are ESR silent.

Before giving proofs for these statements in paper II, we shall here present an overview of the paramagnetic defects found in the studied $BaTiO_3$ single-crystal specimens. For three reasons we strive for completeness in this respect. First, there might be defects with useful photorefractive properties among those identified. Second, the light-induced charge changes observed (also with centres present in small concentrations only) can be used as indicators of the sign and transport properties of the charge carriers created by illumination of the crystals with specific light energies. And finally, the ESR studies, in favourable cases sensitive to the low defect concentrations (tens of ppm) relevant for photorefractive sensibilization of the crystals, can be used as a tool of quality control.

In identifying paramagnetic defects in $BaTiO_3$ we could rely to some extent on previous studies, performed with the related $SrTiO_3$. Most of the the relevant results have been summarized by Müller [6]. The study of paramagnetic defects and their light-induced charge and optical absorption changes is more complicated in $BaTiO_3$, having a sequence of ferroelectric phases (tetragonal: $T \lesssim 393$ K, orthorhombic: $T \lesssim 278$ K, rhombohedral: $T \lesssim 183$ K), in contrast to $SrTiO_3$, which shows only a structural phase transition from cubic to tetragonal at 105 K. Most studies had to be performed at low temperatures in the rhombohedral phase, since many defects have been observed and their different spin–lattice relaxation times would have prevented observation at high temperatures. The temperature dependence of the ESR parameters derived for the various centres has not been studied specifically. Neither did we investigate in detail the redox behaviour of the defects concerning their charge states and photoionization properties.

For previous results on defects in oxide perovskites refer to [6]. Newer investigations on $BaTiO_3$ include those by Müller *et al* on $BaTiO_3$:Mn^{4+} [7] and Cr^{3+} [8]. ESR studies devoted to the elucidation of the photorefractive properties of Co- and Mn-doped $BaTiO_3$ have recently been published by Schwartz *et al* [9]. These investigations, however, were primarily made on doped $BaTiO_3$ powders, yielding

less structural information than studies of single crystals. We have earlier reported several results on paramagnetic defects in single-crystal $BaTiO_3$ and their dependence on light illumination [10]. Further references will be cited in the relevant subsections. In this paper we shall concentrate on newly identified paramagnetic defects and on more detailed recent information about those found previously.

2. Experimental conditions

The crystals used in this investigation are listed in table 1. They were kindly made available by various crystal growers. Most of the specimens were studied as grown. Polydomain samples with dimensions of typically about $1 \times 3 \times 3$ mm^3 were used. Among the identified charge states there were many which could be created metastably at low temperatures by illumination with light of suitable wavelengths. In general, the output of a H_2O filtered xenon arc lamp was used, monochromatized by interference filters. More details will be reported in II.

The ESR measurements were made at 4.2 K $\leqslant T \leqslant$ 300 K, using a Bruker 200 D ESR spectrometer working at 9 and 34 GHz.

3. Experimental results and their assignment

We shall first deal with paramagnetic defects on cation sites—either isolated or associated with oxygen vacancies—and then turn to anion type centres, essentially oxygen ions having trapped a hole, O^-. The spectra are generally described by Hamiltonians of the type [11]

$$\mathcal{H} = \beta \boldsymbol{B}\boldsymbol{g}\boldsymbol{S} + \boldsymbol{I}\boldsymbol{A}\boldsymbol{S} + D[S_{z'}^2 - \tfrac{1}{3}S(S+1)] + E(S_{x'}^2 - S_{y'}^2) + \tfrac{1}{6}a[S_x^4 + S_y^4 + S_z^4 - \tfrac{1}{5}S(S+1)(3S^2+3S-1)] \quad (1)$$

indicating, respectively, Zeeman, hyperfine, axial and orthorhombic as well as cubic crystal field interactions. The coupling tensors and crystal field parameters reflect the local symmetry of the defects and allow conclusions with respect to their electronic structure. In the headings of the subsections we shall indicate the free ion electronic configurations of the identified ions and whether Hund's rules are obeyed for the ion in the crystal (weak cubic crystal field) or not (strong field).

3.1. Defects containing Fe

For all crystals we have found that isolated Fe^{3+} [12] leads to the strongest signals. Fe^{3+}–V_0 [13] was observed only in the Fe-doped material; Fe^{4+}–V_0 [13], however, could also be detected in nominally undoped specimens. Apparently, the Fermi level was so low in such crystals that Fe^{3+}–V_0 was not formed. Fe^{5+} [13] was observed under illumination; details will be published in II.

Table 1. The investigated crystals and their impurity content.

Crystal designation	Doping		Identified defects[a]
57.2	nominally undoped [b] (Si: 250, Fe: 210, Al: 130, K: 120, Ca: 90, Sr: 80, Mg: 50, S: 15, Ni: 12, P: 11, Sn: 8)	−:	$\underline{Fe^{3+}}$, Cr^{3+}, Pt^{3+}, (Al^{3+})
		+:	Fe^{4+}–V_O, Fe^{5+}, Cr_I^{5+}, Cr_{II}^{5+}, Nd^{3+}, $(Nd^{2+/4+?})$
		o:	(Fe^{4+}), (Cr^{4+}), Al^{3+}–O^-, (Pt^{4+})
		u:	O^-–U, Ti^{3+}–?
68.2	nominally undoped	−:	$\underline{Fe^{3+}}$, Cr^{3+}, Co^{2+}, (Co^{3+}), $(Ni^{3+/2+/1+?})$
		+:	Fe^{3+}–V_O, Fe^{4+}–V_O, Fe^{5+}, Cr_I^{5+}, Cr_{II}^{5+}, Nd^{3+}, $(Nd^{2+/4+?})$
		o:	Mn^{4+}, (Fe^{4+}), (Cr^{4+})
		u:	O^-–U, Ti^{3+}–?
73.1	160 ppm Fe, 100 ppm Co in crystal	−:	$\underline{Fe^{3+}}$, Cr^{3+}, $\underline{Co^{2+}}$
		+:	Co^{3+}–V_O, Co^{4+}–V_O, Cr_{II}^{5+},
		o:	(Fe^{4+}), (Cr^{4+})
45.2	400 ppm Fe in crystal	−:	$\underline{Fe^{3+}}$
		+:	Fe^{3+}–V_O, Fe^{4+}–V_O, Fe^{5+}, Cr_I^{5+}, Nd^{3+}, $(Nd^{2+/4+?})$
AK45	nominally undoped	−:	Fe^{3+}, Cr^{3+}
		+:	Fe^{5+}, Cr_I^{5+}
		o:	(Fe^{4+}), (Cr^{4+})
		u:	O^-–U, Ti^{3+}–?, 2, 3
Z3VIII	50 ppm Co in the melt	−:	$\underline{Fe^{3+}}$, Cr^{3+}, $\underline{Co^{2+}}$, (Co^{3+}), Pt^{3+}, $(Ni^{3+/2+/1+?})$
		+:	Fe^{4+}–V_O, Fe^{5+}, Nd^{3+}, Cr_I^{5+}, $(Nd^{2+/4+})$
		o:	Co^{4+}–V_O, (Fe^{4+}), Ir^{4+}, Rh^{4+}, (Pt^{4+}), (Cr^{4+})
		u:	O^-–U, Pt^{5+}–?
04	nominally undoped	−:	Fe^{3+}, Cr^{3+}, Co^{2+}, Pt^{3+}, $\underline{Rh^{2+}}$
		+:	Nd^{3+}, $(Nd^{2+/4+})$
		o:	(Pt^{4+})

[a] Notation: −, acceptor defect; +, donor defect; o, neutral; u, structure and charge unknown; **bold letters**, charge states stable in crystal ground state; light letters, charge states obtained by illumination; elements in brackets, indirectly determined, not by ESR; underlined, especially high concentration. The numbers 2 and 3 refer to table 2.

[b] Mass spectrometric analysis available, results given in at-ppm.

3.1.1. Isolated Fe^{3+} ($3d^5$, weak field). Figure 1 shows a typical spectrum of this ion as investigated in the rhombohedral phase at $T \approx 20$ K. The labelled resonances have been assigned earlier to Fe^{3+} [12] and Cr_I^{5+} [10]. The parameters describing the spectra of Fe^{3+} in the rhombohedral phase at 172 K are listed in table 2. The two sharp lines marked by 'X' have the angular dependence shown in figure 2, where the line positions of the isolated Fe^{3+}, as calculated using the cited parameters are indicated. It is seen that the narrow lines are situated in the region of the fine structure resonances of isolated Fe^{3+}. Analogous observations were made for the rotation of $\boldsymbol{B}$ in a (110) plane of the crystal. More specifically, for $\boldsymbol{B} \parallel [100]$ the positions of the sharp lines divide the distance between the neighbouring fine structure lines in the ratio of about 1 : 2. Spectra of Fe^{3+} in MgO, also showing such

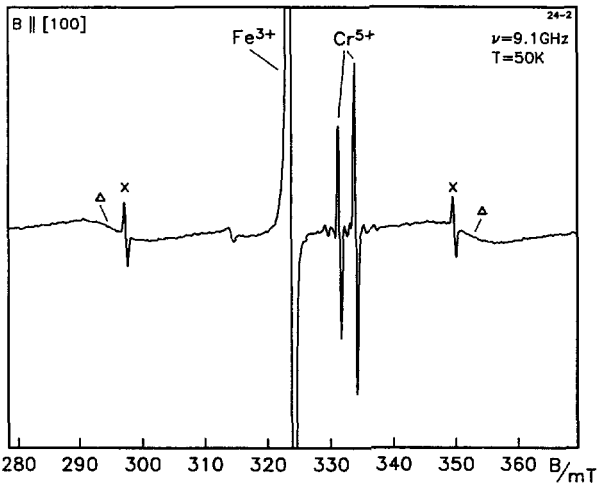

Figure 1. ESR spectrum of a nominally undoped $BaTiO_3$ crystal under the indicated conditions. Δ, X: single and double quantum fine structure transitions of Fe^{3+}, respectively.

sharp structures, have first been reported by Auzins and Wertz [14]. The narrow lines were assigned without doubt to the subsequent absorption of two equal quanta in the transitions $|m_s = -5/2\rangle \leftrightarrow |-3/2\rangle$ and $|1/2\rangle \leftrightarrow |3/2\rangle$ as well as between the time conjugate states. Two features of these resonances are remarkable: The two subsequent transitions do not involve a common level. Thus after absorption of the first quantum, exciting Fe^{3+} for instance from $|-5/2\rangle$ to $|-3/2\rangle$, the system has to be promoted, possibly by a phonon, to $|1/2\rangle$ before the next quantum can be absorbed. Second, the two transitions do not occur at the same magnetic field, if the influence of tetragonal strains is neglected ($D = 0$):

$$\begin{aligned} g\beta B &= h\nu + 2a + 4D && |-5/2\rangle \leftrightarrow |-3/2\rangle \\ g\beta B &= h\nu + \frac{5}{2}a - 2D - \frac{5}{16}\frac{a^2}{h\nu} && |+1/2\rangle \leftrightarrow |+3/2\rangle. \end{aligned} \tag{2}$$

Only if Fe^{3+} is situated in an environment which is tetragonally strained ($D \neq 0$) in such a way that both fields coincide does the probability for the simultaneous absorption of two quanta rise strongly. For the two resonances to occur at identical field values the upper transition in equation (2) has to lie at $4D$ higher than the normal one ($D = 0$) and the second transition at $2D$ lower. The double quantum resonances thus are predicted to divide the field distance between the cubic fine structure levels in the ratio 1:2. The sharpness of the resonances results from the fact that this condition for resonance at equal magnetic field is fulfilled only for specific Fe^{3+} ions which are situated in environments showing just the needed tetragonal distortions, and not for all Fe^{3+} ions. These resonances thus are site selective. In contrast the single quantum fine structure transitions, marked 'Δ' in figure 1, are caused by Fe^{3+} in all possible strained environments. Apparently, the investigated $BaTiO_3$ crystals contained wide distributions of tetragonal strains as indicated by the broadness of the normal fine structure transitions at $B \parallel [100]$ in figure 1. For this orientation only tetragonal strains and not trigonal ones can shift the line positions. It should be added that the ratio of the intensities of the sharp

Table 2. Paramagnetic defects in the investigated $BaTiO_3$ crystals and their spectral parameters.

Ion	T (K)	g^a	A (cm^{-1})	D (cm^{-1})	E (cm^{-1})	a (cm^{-1})	Remarks	Reference
Ti^{3+}–$?_I$	20	$g_{[001]+\tau}$: 1.938(1) $g_{[010]+\tau}$: 1.926(1) $g_{[100]}$: 1.913(1)					$\tau = 26(2)°$ (rotation from [001] to [010])	present paper
Ti^{3+}–$?_{II}$	20	$g_{[001]+\tau}$: 1.937(1) $g_{[110]}$: 1.931(1) $g_{[1\bar{1}0]+\tau}$: 1.898(1)					$\tau = 12.5(7)°$ (rotation around [110])	present paper
Ti^{3+}–$?_{III}$	20	$g_{[001]+\tau}$: 1.937(1) $g_{[110]}$: 1.933(1) $g_{[1\bar{1}0]+\tau}$: 1.899(1)					$\tau = 13.1(7)°$ (rotation around [110])	present paper
Cr^{3+}	18	1.980(2)		0.025(2)				[8]
Cr_I^{5+}	18	$g_{[001]}$: 1.934(1) $g_{[110]}$: 1.952(1) $g_{[1\bar{1}0]}$: 1.959(1)	0.00111(3) 0.00075(5) 0.00348(3)					[10]
Cr_{II}^{5+}	75	$g_{[001]}$: 1.945(1) $g_{[110]}$: 1.955(1) $g_{[1\bar{1}0]}$: 1.988(1)	$A_{[001]}$: 0.0026(2) $A_{\perp[001]}$: 0.0012(1)					present paper
Mn^{4+}	4.2	$g_{\parallel[111]}$: 1.9968(19) $g_{\perp[111]}$: 2.0015(5)	0.006748(5) 0.007304(15)	0.65(1)				[7]
Fe^{3+}	172	2.003(2)		−0.0023(5)		0.0113(10)		[12]
	20	2.005(3)		−0.0019(5)		0.0103(10)		present paper
Fe^{3+}–V_O	20	$g_{[001]}$: 2.00(1) $g_{[110]}$: 5.71(1) $g_{[1\bar{1}0]}$: 6.26(1)		1.04(5)	0.016(5)		$\tau = 0.8(2)°$	[13]

Fe^{4+}–V_O	10	$g_{\|[100]}$: 2.010(5) $g_{\text{eff}\perp[100]}$: ≈ 0			0.279(2)	$\tau = 0.8(2)°$	[13], present paper
$SrTiO_3$:Fe^{4+}–V_O	4.2	$g_{\|[100]}$: 2.007(1) $g_{\text{eff}\perp[100]}$: ≈ 0			0.1504(8)	$\tau = 1.35°$	[15]
Fe^{5+}	20	$g_{\|[111]}$: 2.010(3) $g_{\perp[111]}$: 2.013(3)		1.15(5)		$\tau = 1.0(2)°$	[13]
Co^{2+}	20	$g_{\|[111]}$: 4.262(5) $g_{\perp[111]}$: 4.346(5)	0.00997(10) 0.01045(10)				present paper
Co^{2+}	4.2	4.347	0.0109				[17]
MgO:Co^{2+}	4.2	4.278(1)	0.00977(2)				[16]
Co^{4+}–V_O	15	$g_{\|[100]}$: 1.885(8) $g_{\perp[100]}$: 1.824(8)	0.0074(2) 0.0092(2)	⩾ 9			present paper
$SrTiO_3$:Co^{4+}–V_O	4.2	$g_{\|[100]}$: 1.8530(5) $g_{\perp[100]}$: 1.8181(5)	0.00839(5) 0.0092(1)	3.05(1)			[23]
$KNbO_3$:Co^{2+}–V_O	20	$g_{\|[100]}$: 2.056(5) $g_{\perp[100]}$: 5.020(10)	0.0063(2) 0.099(2)				[20]
Rh^{2+}	25	$g_{\|[100]}$: 2.030(1) $g_{\perp[100]}$: 2.298(1) g_{av}: 2.210(1)	0.0005(2) 0.0015(2)				present paper
MgO:Rh^{2+}	20	2.1718(2)	0.00127(1)				[31]
Rh^{4+}	25	$g_{\|[111]}$: 1.386(1) $g_{\perp[111]}$: 1.461(1)	0.0026(1) 0.0026(1)			k=0.58	present paper
MgO:Rh^{4+}	20	1.668(1)	0.00325(10)			k=0.75	[31]

[a] The subscripts generally indicate the principal directions.

Table 2. *Continued.*

Ion	T (K)	g[a]	A (cm^{-1})	D (cm^{-1})	E (cm^{-1})	a (cm^{-1})	Remarks	Reference
Ir^{4+}	25	$g_{\parallel[111]}$: 1.575(1) $g_{\perp[111]}$: 1.594(1)	0.0023(1) 0.0023(1)				k=0.69	present paper
MgO:Ir^{4+}	77	1.738(1)	^{191}Ir: 0.00250(5) ^{193}Ir: 0.00267(5)				k=0.80	[32]
Pt^{3+}	9	$g_{[001]}$: 1.958(5) $g_{[110]}$: 2.452(5) $g_{[1\bar{1}0]}$: 2.458(5)	0.0015(3) 0.0111(3) 0.0112(3)					present paper
	4.2	$g_{\parallel[100]}$: 1.950(5) $g_{\perp[100]}$: 2.459(3)	0.0000(5) 0.0135(5)					[25]
Pt^{5+}	25	$g_{[100]}$: 1.35(2) $g_{[010]+\tau}$: 1.31(2) $g_{[001]+\tau}$: 2.05(8)	0.0229(5)				$\tau = 33(2)°$ (rotation from [001] to [011]) $k = 0.68$	present paper
Nd^{3+}	8	$g_{\parallel[111]}$: 2.461(2) $g_{\perp[111]}$: 2.583(2)	^{143}Nd: 0.0246(20) ^{145}Nd: 0.0155(15) ^{143}Nd: 0.0256(20) ^{145}Nd: 0.0162(15)					[35]
1	20	2.248(1)					possibly Ni (1+,2+,3+?)	present paper
2	20	$g_{[001]}$: 1.882(1) $g_{[110]}$: 1.807(1) $g_{[1\bar{1}0]}$: 1.804(1)					$\tau = 0.8(2)°$ model unknown	present paper
3	23	$g_{\parallel[111]}$: 3.390(2) [b] $g_{\perp[111]}$: 4.240(2)					model unknown	present paper

[a] The subscripts generally indicate the principal directions.
[b] Subscripts possibly to be interchanged.

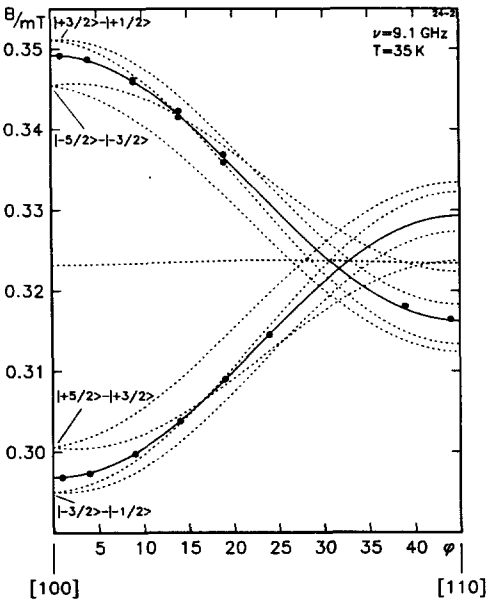

Figure 2. Angular dependence of the single (broken curves) and double quantum (full curves: theory; points: experiment) fine structure transitions of Fe^{3+} in $BaTiO_3$.

fine structure transitions to those of the wide ones varies from crystal to crystal, in accord with strain distributions differing from specimen to specimen.

3.1.2. Fe^{4+}–V_0 ($3d^4$, weak field). This defect leads to strongly angular-dependent signals with $g_{\|\text{eff}} \approx 8$ for $\nu \approx 34$ GHz and $g_{\perp\text{eff}} \approx 0$ [13]. The subscripts refer to the principal axes of the centre extending nearly along [100] directions. There is a slight tilting by $(0.8 \pm 0.2)°$ of the principal axes towards the [111] rhombohedral domain directions. Because of the strong tetragonal field caused by V_0, the orbital degeneracy of the ^5E groundstate of Fe^{4+} is lifted. The spin degeneracy ($S = 2$) is also removed by the tetragonal field, so that only $|m_s|$ remains a good quantum number. The resonances are caused by transitions between the $|m_s = \pm 2\rangle$ levels; their zero field splitting originates from the cubic part of the crystal field. So the resonance condition is given by [15]

$$h\nu = [(4g_{\|}\beta B\cos\theta)^2 + a^2]^{1/2} = g_{\text{eff}}\beta B. \tag{3}$$

Recently we succeeded in detecting the resonance of Fe^{4+}–V_0 also at 9 GHz, in addition to previous measurements at 34 GHz [13]. At 9.1 GHz $g_{\|\text{eff}} = 21.1$ was found as compared to $g_{\|\text{eff}} = 8.3$ at 34.1 GHz. From these values $g_{\|} = 2.010$ and $a = 0.279$ cm^{-1} are determined. These are similar to the corresponding numbers for the well established Fe^{4+}–V_0 in $SrTiO_3$ ($g_{\|} = 2.007$, $a = 0.150$ cm^{-1}), see table 2. This supports the identification of Fe^{4+}–V_0 in $BaTiO_3$. Previously, there remained the open question as to whether Fe^{2+}–V_0 had been observed, since it was expected to lead to similar spectra. This can now be ruled out since the Fermi level in the as-grown crystals is generally so low that even Fe^{3+}–V_0 is not observed sometimes.

3.2. Co related defects

Co doping has recently been found to increase the photorefractive sensitivity of $BaTiO_3$ [9]. An investigation of the structure and optical properties of the defects induced by incorporation of Co will therefore be presented.

3.2.1. Isolated Co^{2+} ($3d^7$, weak field). The spectrum of Co^{2+} for $\boldsymbol{B} \| [111]$ is shown in figure 3. Two closely spaced sets of eight hyperfine lines with relative weights of 1:2.2 are seen. These can be attributed in a natural way to a superposition of resonances in rhombohedral [111] domains and those in $[\bar{1}11]$, $[1\bar{1}1]$ and $[11\bar{1}]$ domains, not all of them being present with equal strengths. The weak distortions along the domain axes will lead to small deviations from the cubic case. Accordingly, the anisotropies of g and A are small: $g_{\|} = 4.262$, $g_{\perp} = 4.346$, $A_{\|} = 99.7 \times 10^{-4}\ cm^{-1}$, $A_{\perp} = 104.5 \times 10^{-4}\ cm^{-1}$. These values are close to those of, e.g., Co^{2+} in MgO [16]. An averaged g has been reported earlier by Žďánský *et al* [17] for $BaTiO_3$:Co^{2+} (see table 2). The angular dependence of the spectra is in full accord with the model, that Co^{2+} is trigonally distorted along the domain axes. This is seen, for instance, by the reconstruction of the resonance positions for $\boldsymbol{B} \| [100]$, where the spectra of all [111]-type domains coincide, with the above parameters, see figure 4.

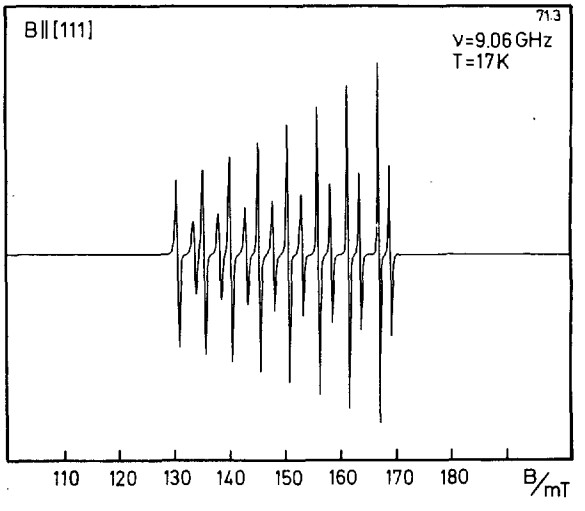

Figure 3. ESR of isolated Co^{2+} in $BaTiO_3$. The two sets of eight lines correspond to Co^{2+} in rhombohedral [111] domains oriented parallel to $\boldsymbol{B}$ (low intensity) and at about 110° to $\boldsymbol{B}$.

The spin–orbit groundstate of Co^{2+} ($S = 3/2$) in a cubic or nearly cubic environment, on which the ESR experiments are performed, results from coupling the spin ($S = 3/2$) to the effective angular momentum ($L = 1$) of the T_1 orbital groundstate, leading to a total angular momentum of $J = 1/2$ in the groundstate and to $g = \frac{1}{3}(10 - 2\alpha k)$ [11] ($\alpha = -1.4$: orbital Landé factor [16]; k: orbital reduction factor). The average of the experimental g-values is reproduced in the present case with $k = 0.918$. This is unusually high. Spin–orbit admixtures of higher orbitals [18,19], not considered here, will lead to slightly positive g-shifts, decreasing the k necessary to explain the experimental g_{av}.

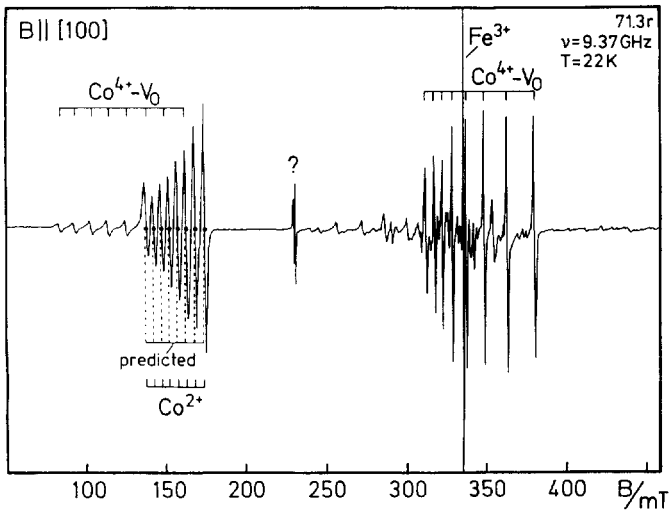

Figure 4. ESR spectra of Co-doped $BaTiO_3$ containing the indicated paramagnetic defects. The line positions of isolated Co^{2+} have been predicted by the parameters also describing the resonances in figure 3 (see text and table 2).

A completely contrasting explanation of the ESR of Co^{2+} in $BaTiO_3$ has been put forward by Aguilar [20]. By taking into account only the spin part of Co^{2+} ($S = 3/2$) in discussing his spectra, he apparently discards spin–orbit coupling. Furthermore, strong [100] tetragonal distortions induced by random strains are assumed. The existence of two sets of eight lines in the spectra for $B \| [111]$, as shown in figure 3, is then attributed to second order splitting between the $|m_s = \pm 3/2\rangle$ and $|m_s = \pm 1/2\rangle$ substates caused by the assumed strong axial field. These arguments cannot hold, first because the angular dependence of the spectra can only be explained by a weak [111] distortion of the centres, as indicated by the reconstruction of their angular dependences, part of which is shown in figure 4. Second, strongly tetragonally distorted Co^{2+} centres lead to quite different spectra, as will be shown now in the course of discussing the newly found resonances of Co in tetragonal symmetry in $BaTiO_3$.

3.2.2. Co^{4+}–V_0 ($3d^5$, weak field). Several strong Co related resonances with pronounced tetragonal anisotropy have been identified. Not all of them could be attributed to definite models yet, but it is likely that Co^{2+}–V_0, Co^{3+}–V_0 and Co^{4+}–V_0 are among these centres, appearing under various illumination conditions and temperatures. Because of the multitude of all the detected tetragonal Co defects, partly unassigned, we plan to give a separate review, concentrating here on Co^{4+}–V_0, which is most clearly observed under illumination.

We first differentiate the spectral parameters of this centre from those of Co^{2+}–V_0 because of the final remarks in the preceding section. The spin-Hamiltonian parameters of Co^{2+}–V_0 in $KNbO_3$ [19] are listed in table 2. They are similar to those of the tetragonal centre reported here (table 2). For Co^{2+}–V_0, $g_\parallel \approx 2$ and $g_\perp \approx 5$, expected for Co^{2+} in a strong tetragonal crystal field. The total angular momentum, J, is no longer a good quantum number, only $|m_J|$. If the sign of the tetragonal field is such that an orbital singlet is lowest, pulled down from the cubic T_1 groundstate, then the orbital angular momentum tends to be quenched and for the

extreme case of a spin-only, $|m_s = \pm 1/2\rangle$, groundstate $g_{\parallel} \approx 2$, $g_{\perp} \approx 4$ is expected for a $S = 3/2$ spin system. The g-values of Co^{2+}–V_0 therefore correspond to the not quite complete quenching of orbital angular momentum. The analysis of the spectral parameters for the general case has been elaborated by Abragam and Pryce [18].

It turns out, however, that the present axial Co spectra cannot be explained consistently by this theory. This discrepancy is accentuated by the fact that two tetragonal Co centres have been discovered recently in one crystal of $KTa_{0.9}Nb_{0.1}O_3$ [21]. One of them shows spectral features specific for Co^{2+}–V_0; the other one, parameters comparable to those of the present tetragonal Co centre. So indeed these spectra are caused by a different defect centre. We assign them to Co^{4+}–V_0, assuming a weak field configuration ($3d^5$, $t_2^3e^2$, $S = 5/2$). The strong axial perturbation by V_0 will lead to three Kramers doublets, the lowest having $g_{\parallel} \approx 2$, $g_{\perp}^{\text{eff}} \approx 3g_{\perp} \approx 6$ [22], if the splitting, D, between the two lowest Kramers doublets is large compared to the microwave quantum $h\nu$. Deviations for $g_{\perp}^{\text{eff}}$ occur if $D \approx h\nu$; then $g_{\perp}^{\text{eff}} = 3g_{\perp}(1 - \frac{1}{2}(g_{\perp}\beta B/D)^2)$ [22]. From measurements at frequencies of 9.06 GHz and 33.9 GHz we find $g_{\parallel} = 1.885$, $g_{\perp} = 1.824$ and $D \geqslant 9$ cm^{-1}. Similar resonances (table 2), characterized by $g_{\parallel} = 1.8530$, $g_{\perp} = 1.8181$, $D = 3$ cm^{-1} [23], have been found in $SrTiO_3$ and assigned to Co^{4+}–V_0. This supports our model.

3.3. Pt^{3+} ($5d^7$, strong field), Rh^{2+} ($4d^7$, strong field)

Pt^{3+} has been investigated earlier in $BaTiO_3$ [24–28]. It was found that this ion assumes the strong field configuration (t_2^6e) and thus has a single unpaired spin ($S = 1/2$) moving in an E-type orbital groundstate. ^{195}Pt (34% natural abundance) has nuclear spin $I = 1/2$; the remaining isotopes, $I = 0$. The crystal environment of Pt^{3+} is essentially tetragonally distorted along [100]-type directions. This is a manifestation of a static E × e Jahn–Teller effect [28]. A slight perturbation, caused by the [111] domain field, is superimposed, leading to orthorhombic symmetry.

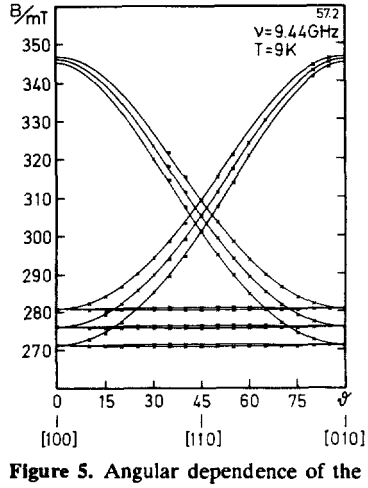

Figure 5. Angular dependence of the ESR of Pt^{3+} in $BaTiO_3$, reproduced from the parameters of table 2, determined in the present investigation. Note the slight orthorhombic splittings of the low field lines and the finite hyperfine splitting ($A_{\parallel} = 15 \times 10^{-4}$ cm^{-1}) for $\boldsymbol{B} \parallel [010]$ near 346 mT.

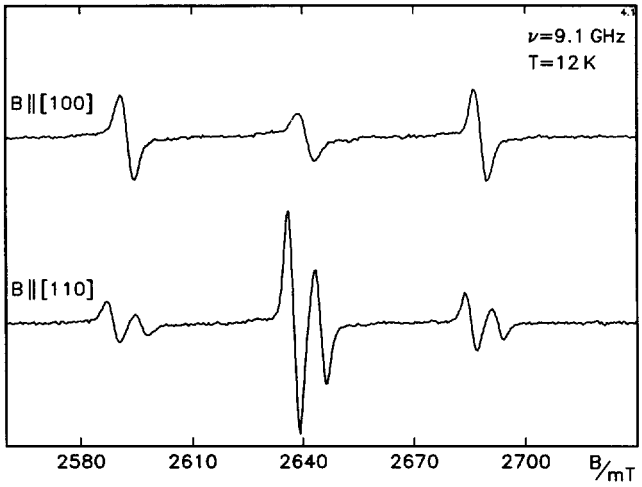

Figure 6. Angular dependence of the line intensities of ^{195}Pt ($I = 1/2$; outer peaks) and the remaining Pt^{3+} ions having $I = 0$ (central peak).

We report the investigation of Pt^{3+} anew because the previous results [24,26] are at variance with those obtained by us. Figure 5 shows the angular dependences of the spectra as compared to the their prediction using the parameters shown in table 2. They are contrasted there to those reported by Šroubek *et al* [24]. Discrepancies between both sets of data, which are outside the limits of error, are clearly seen. Figure 5 demonstrates, for instance, that the hyperfine splitting for $B \| [100]$, $A_{\|}$, is larger than zero in contrast to [25]. Excluding the unlikely possibility, that Pt^{3+} occurs in two slightly different electronic configurations in $BaTiO_3$, we think that the present results are more accurate, possibly because of the recent availability of crystals of higher quality, as indicated, e.g., by their comparatively narrow lines, see figure 6. It should be remarked, however, that the parameters given in [25], where no resonances are shown, are not in accord with the spectra exhibited in the previous publication [24].

Of special interest is the intensity of the hyperfine doublet, $I = 1/2$, in figure 6 relative to that of the central $I = 0$ line. For $B \| [100]$ the height of the latter resonance at 12 K and 2 mW microwave power is unexpectedly lower than that of the hyperfine doublet. The ratio 1:3.9 of each of the hyperfine lines to the central line, as calculated from the natural abundances of the respective isotopes, is approached, if B is turned away from [100], if the temperature is raised or if the microwave power is decreased. The unexpected intensity ratio thus has to be attributed to saturation depending on angular and nuclear spin. It will be shown that these effects are a vivid demonstration of spin–lattice relaxation accompanying reorientation within a static E × e Jahn–Teller system [29].

We first consider the angular dependence of the height of the central line ($I=0$). For an explanation we take into account the static Jahn–Teller [100] type distortions of the Pt^{3+} surroundings. The Zeeman effect in each of these wells is characterized by an anisotropic g-tensor having principal axes along the distortion axis and perpendicular to it. Because of this anisotropy, the quantization axes of the unpaired spin change if the system reorients between equivalent wells. Phonon-induced reorientation is thus in general connected with spin relaxation. This process is absent for $B \| [100]$, for

under this orientation the quantization axes do not change, B being normal to all g-tensor ellipsoids in all wells. Accordingly, the spin–lattice relaxation time T_1 is angular dependent, as observed. Ham [30] gives the following expression for T_1:

$$T_1^{-1} = \frac{2}{3}\left(\frac{\Delta g\beta B + \Delta A m}{h\nu}\right)^2 (\zeta_x^2\zeta_y^2 + \zeta_y^2\zeta_z^2 + \zeta_z^2\zeta_x^2)\tau^{-1} \qquad (4)$$

where τ is the reorientation time, Δg and ΔA are the anisotropic parts of the Zeeman and hyperfine tensors, respectively, and ζ_i represent direction cosines with respect to [100]-type directions.

It now remains to explain the spin–lattice relaxation time of the hyperfine doublet, which is shorter than that of the central line also for $B \| [100]$. Anisotropic hyperfine interaction in this Jahn–Teller system can lead to spin–lattice relaxation [30] also for $B \| [100]$, in addition to a process having the same angular dependence as the relaxation via g-tensor anisotropy, see equation (4). This mechanism is also connected with the change of the spin quantization axes under reorientation, this time being caused by the off-diagonal terms of the hyperfine interaction, proportional to $I_x S_x$ and $I_y S_y$. The electron spin–lattice relaxation here is accompanied by a nuclear spin flip [30].

An isotropic spectrum of Pt^{3+}, originating from fast reorientation at elevated temperatures, has been observed earlier [27] in crystals in which the charge state Pt^{3+} had been stabilized by Nb doping. In our case Pt^{3+} was metastably created by illumination, and an isotropic spectrum could not be observed since recombination to the crystal ground state occurred at lower temperatures than a sufficiently fast reorientation rate.

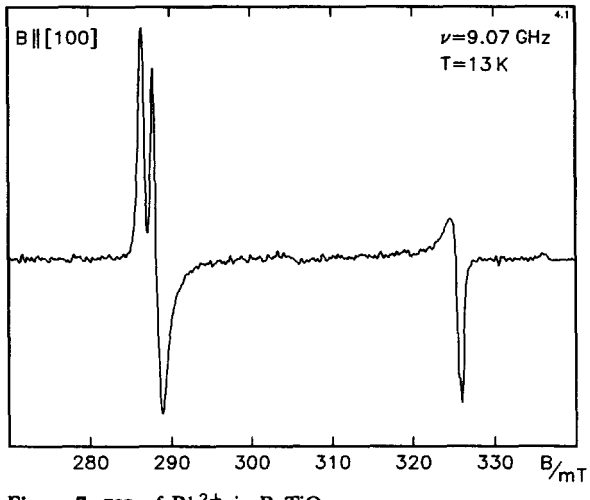

Figure 7. ESR of Rh^{2+} in $BaTiO_3$.

Figure 7 shows resonances which we attribute to Rh^{2+} on account of their characteristic doublet hyperfine structure (^{103}Rh, 100% $I = 1/2$) and by comparison with the analogous spectra of Rh^{2+} in MgO [31], table 2. It should be remarked, that it is generally difficult to distinguish the ESR of octahedral (nd^7) strong field configurations from those of (nd^9), corresponding to Rh^0 ($4d^9$). However, the observation of

Rh^{4+} in another $BaTiO_3$ crystal (section 3.4) supports the assignment of the present spectra to Rh^{2+} since it is unlikely that in such crystals, both grown under oxidizing conditions, the charge state of a defect ion varies by four. The angular dependence of the Rh^{2+} lines, characteristic for [100] tetragonal symmetry, is shown in figure 8. The electronic configuration of Rh^{2+} is analogous to that of Pt^{3+}, and the observed tetragonality again is caused by an E × e Jahn–Teller effect. Since Rh^{2+} is stable in the investigated crystal, motional averaging by fast reorientation could be observed at 46 K for all crystal orientations, the resulting linewidths being strongly dependent on angle, as predicted [30].

Pt and Rh as well as Ir, to be reported in the next section, probably entered the investigated specimens from the Pt, Pt–Rh and Ir crucibles and wires used in growing the respective crystals.

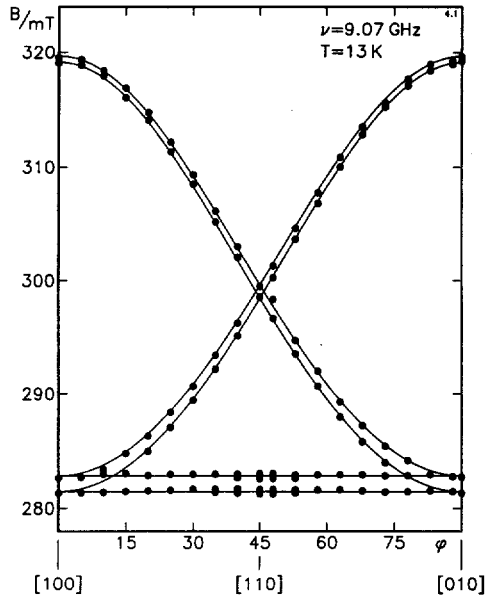

Figure 8. Angular dependence of the ESR of Rh^{2+} in $BaTiO_3$.

3.4. Rh^{4+} ($4d^5$), Ir^{4+} ($5d^5$), Pt^{5+}–? ($5d^5$) (all strong field)

Figure 9 shows the spectra of these ions for $B \| [111]$, which were all observed in the same crystal. Rh^{4+} and Ir^{4+} were detected without illumination. The different ions are characterized by their typical hyperfine patterns, as described above for Pt^{3+} and Rh^{2+}. Ir^{4+} has two stable isotopes, ^{191}Ir and ^{193}Ir, with 37% and 63% natural abundance, respectively. Both have $I = 3/2$ and almost equal nuclear moments. So the hyperfine pattern of Ir^{4+} consists of four nearly equally intense lines. The splittings into two sets of lines for Rh^{4+} and Ir^{4+} are consistent with the axial symmetry of the centres along the [111] rhombohedral domain directions. The deviation of the intensity ratio of the two sets in each case from the expected relations, 1:3, indicates that the rhombohedral domains were present in the crystal with unequal strengths. Since the deviations from cubic symmetry are small for Ir^{4+} and Rh^{4+}, we shall discuss their properties on the basis of an octahedral environment. Note, Pt^{5+} shows a larger and slightly orthorhombic distortion away from cubic symmetry; this

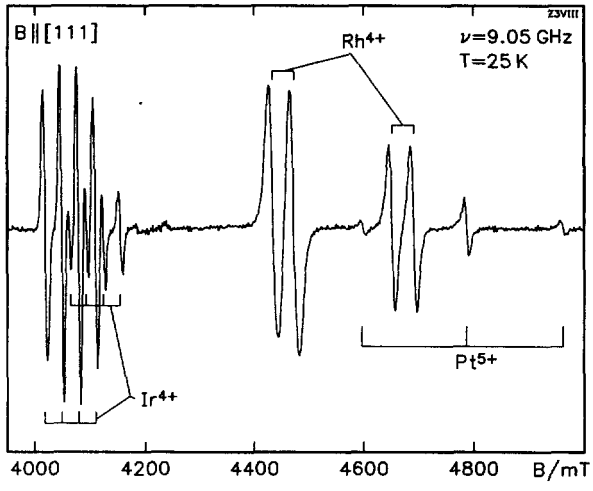

Figure 9. ESR spectra of Ir^{4+}, Rh^{4+} and Pt^{5+} in $BaTiO_3$.

and the orientation of one of the principal axes along the rather unusual direction of 30° away from [100] in a (100) plane points to the association of a defect, so far unknown, with Pt^{5+}.

Let us first discuss the features of Ir^{4+} and Rh^{4+}. The strong field (nd^5) configurations (t_2^5) have a T_2 orbital groundstate ($L = 1$, orbital Landé factor [11]: $\alpha = -1$), to which an unpaired spin ($S = 1/2$) is coupling, forming $J = 1/2$ in the groundstate. The situation is analogous to spin–orbit coupling and the anomalous Zeeman-effect of the p states of an alkali atom, leading to $g = -1/3(g_s - 4\alpha k)$ for $J = 1/2$ (k: orbital reducion factor; $\alpha = 1$ and $k = 1$ in the case of an alkali atom). The values of k, explaining the experimental average g-values for Ir^{4+} and Rh^{4+} in $BaTiO_3$, are listed and compared to those of MgO:Ir^{4+} [32] and MgO:Rh^{4+} [31] in table 2. Admixtures of higher states [33] leads to small increases of g beyond those predicted by the above relation. The k-values in table 2 thus have to be considered as upper bounds for the real ones. It should be noted that the high spin–orbit coupling constants of the three ions treated here stabilize these systems against Jahn–Teller distortions [34]. For further comparisons with Ir^{4+} in other oxide compounds see [19].

To our knowledge Pt^{5+} has not been identified so far by ESR. Considering the nearly axial strong distortion of the centre, we shall show that the g-tensor can be explained on the basis of a strong field ($5d^5$, t_2^5) configuration. Abragam and Bleaney [11] list for this case:

$$g_{\|} = g_s \sin^2\alpha - (g_s + 2k)\cos^2\alpha$$
$$g_{\perp} = -g_s \sin^2\alpha - 2\sqrt{2}k\cos\alpha\sin\alpha \qquad (5)$$

where α is the angle describing mixing with excited orbital states. Coincidence with the experimental axially averaged g-values is found for $k = 0.69$ with $\alpha = 29.7°$.

Since Pt^{5+} by itself is positively charged with respect to Ti^{4+}, it is expected that the symmetry lowering associated defect is not adding to the charge unbalance, i.e., it is either neutral or charged negative with respect to the lattice. No further information on this defect is available presently.

3.5. Further paramagnetic cation centres in $BaTiO_3$.

For the sake of completeness we mention here also the cation type defects which we additionally observed by ESR in the available specimens. These include, first, those about which no further information beyond that previously known was obtained and, second, those which cannot yet be assigned to definite models.

The following ions belong to the first set: Cr_I^{5+} [10], Cr^{3+} [8], Mn^{4+} [7], Nd^{3+} [35]. The relevant ESR parameters are included in table 2. The Cr^{5+} ion we have observed previously [10] is labelled Cr_I^{5+} in table 2. Recently we have detected another defect containing Cr, as identified by its hyperfine structure. We attribute it to Cr^{5+} because of the similarity of its g-values (Cr_{II}^{5+} in table 2) to those of the Cr_I^{5+}. Furthermore, several similar Cr^{5+} centres have clearly been identified in $SrTiO_3$ [36,37].

The second class encompasses a family of centres designated Ti^{3+}–?, and those labelled 1, 2 and 3 in table 2. The assignment of Ti^{3+}–? is made on the basis of the g-tensors of these centres, having g-shifts typical for Ti^{3+} [38]. The low symmetries of the centres point to association with various lattice perturbations of so far unknown structure. Two additional defects of this type have previously been assigned [39] to oxygen vacancies which have trapped one electron; it is expected to be localized at one of the two Ti ions next to the oxygen vacancy. Such defects should, however, show pure axial [100]-type symmetry. The fact that several types of lower symmetry have been observed, contradicts the assignment to an oxygen vacancy. On the other hand, the presence of oxygen vacancies in differently distorted regions of different structure in the crystals or associations with further defects cannot be ruled out either. It should be mentioned that these Ti^{3+}–? signals are weak and that they appear only after illumination with light energies close to the bandgap.

Centre 1 has an isotropic g-value characteristic for Ni in the charge states 1+, 2+ or 3+ [40]. Unfortunately, all these electronic configurations can lead to nearly identical g-factors [40]. A further discrimination is therefore not possible at present. No model is currently conceivable to explain defects 2 and 3.

4. Paramagnetic defects with anion character, O^- trapped hole centres

As will be shown in II, many of the cation type defects described above form deep levels from which holes are photoionized to the valence band in as-grown and oxidized material. In this section, newly found O^- trapped hole centres will be described which in some crystals lead to the shallow levels necessary to explain the charge transport properties of $BaTiO_3$ at low temperature.

4.1. Trapped hole centre I, O^- in unidentified surroundings

After illuminating nominally undoped $BaTiO_3$ crystals with wavelengths $\Lambda \leqslant 600$ nm strong spectra appeared, their angular dependence being given in figure 10. On account of their characteristic g-shifts, $0 \leqslant \Delta g \leqslant 0.11$, these resonances are attributed to a family of closely related O^- hole centres [41]. The contribution of several different defects is demonstrated by the behaviour of the signals under isochronal anneal, figure 11. The crystals were illuminated at 15 K, then heated to the temperatures indicated in figure 11, held there for 2 min, cooled and measured at 15 K. This cycle was repeated without prior illumination for all the successive temperatures indicated.

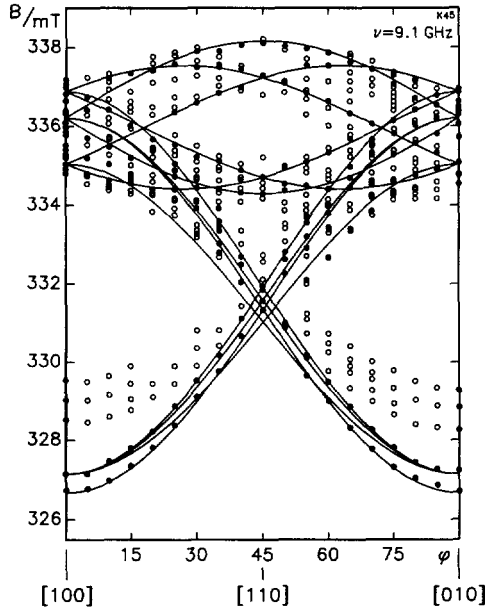

Figure 10. Angular dependences of the ESR spectra of O^- trapped holes in illuminated nominally undoped $BaTiO_3$. Open circles: line positions of centres decaying below 60 K. Full circles and curves: experimental and theoretical positions of remaining centres (O_c^-, see table 3).

Figure 11 shows that there are three decay thresholds; centres of type O_a^- are the shallowest with the strongest decrease near 25 K. Then follows O_b^- with the decrease near 40 K and a group of three centres, O_c^-, decaying together near 65 K. It should be noticed that the holes thermally ionized from O_a^- are partly captured by the O_b^- and O_c^- as indicated by the increase of the latter two near the threshold of O_a^- in figure 11. This shows that the holes created by photoionization of deep centres at low temperatures are trapped with an exceptionally high capture cross section at the shallowest, O_a^-, centres.

The angular dependence of the three partners of the O_c^- subfamily are indicated by full circles in figure 10, some of those decaying at lower temperatures, by open circles. Only the O_c^- spectra have been analysed more closely. They are described by the g-tensors given in table 3.

It has been demonstrated earlier [10], that the orbital model shown in figure 12 is consistent with the structure of these g-tensors. The most decisive observation is the large Δg_x. Since $\Delta g_x \approx -2\lambda / E_y$, where E_y is the energy for the virtual excitation from the p_z groundstate to p_y, the high g_x points to the near degeneracy of the p_z and p_y orbitals. This argues against a Ba-vacancy, V''_{Ba}, as the trapping acceptor. An acceptor ion on a Ti site, A'_{Ti}, would be consistent with the small energy difference between the p_x and p_y states. It is hard to imagine, however, how such a definite trapping centre can lead to the observed variety of O^- centres. Self-trapping of holes at O^{--} in slightly different surroundings cannot be excluded. The various trapping sites can possibly be attributed to a distribution of internal strains.

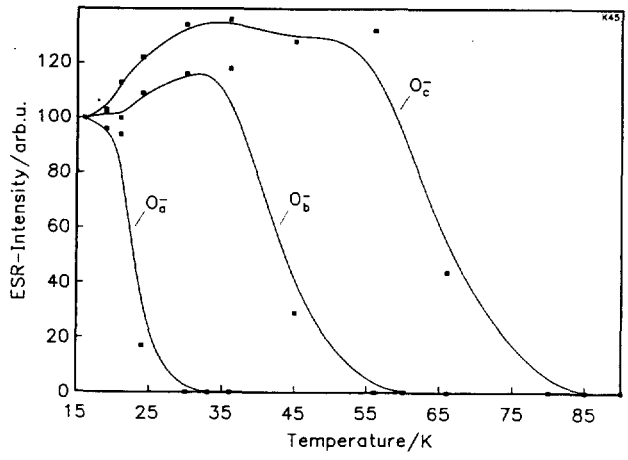

Figure 11. Isochronal anneal (see text) of O^- trapped hole centres in nominally undoped $BaTiO_3$.

Table 3. O^- trapped hole centers in the investigated $BaTiO_3$ crystals and their spectral parameters.

Ion	T (K)	g	A (cm^{-1})	Remarks
O_{cI}^-	20	g_1: 2.072(1) g_2: 2.027(1) g_3: 2.008(1)		$\alpha' = 27(2)°$ (figure 12)
O_{cII}^-	20	$g_{[001]}$: 2.075(1) $g_{[110]}$: 2.028(1) $g_{[1\bar{1}0]}$: 2.005(1)		$\alpha = 45(1)°$
O_{cIII}^-	20	$g_{[001]}$: 2.072(1) $g_{[110]}$: 2.028(1) $g_{[1\bar{1}0]}$: 2.005(1)		$\alpha = 45(1)°$
Al^{3+}–O^-	18	$g_{[110]}$: 2.049(1) $g_{[001]}$: 2.026(1) $g_{[1\bar{1}0]}$: 2.013(1)	0.0008(1)	see figure 12

4.2. Trapped hole centre II, O^-–Al^{3+}

In another nominally undoped crystal, it was identified that holes created by low-temperature illumination were captured at O^- ions next to Al_{Ti}^{3+}. Figure 12 also shows a model of this defect. In contrast to the previous family of O^- centres, here only one type of spectrum, figure 13, was observed, accentuating that the multitude of centres found above is unlikely to have a definite ion to which it is bound but rather sits in differently distorted surroundings. The g- and A-tensors describing the present situation are also given in table 3. Note that ^{27}Al (100% abundance) has nuclear spin $I = 5/2$.

In interpreting the tensor elements we start with the observation that the components of g have the small positive g-shifts expected for O^- trapped holes [41], which were also identified for instance in the previous case. The isotropic hyperfine interaction with Al is rather small, a situation typical [42] for Al lying on or near

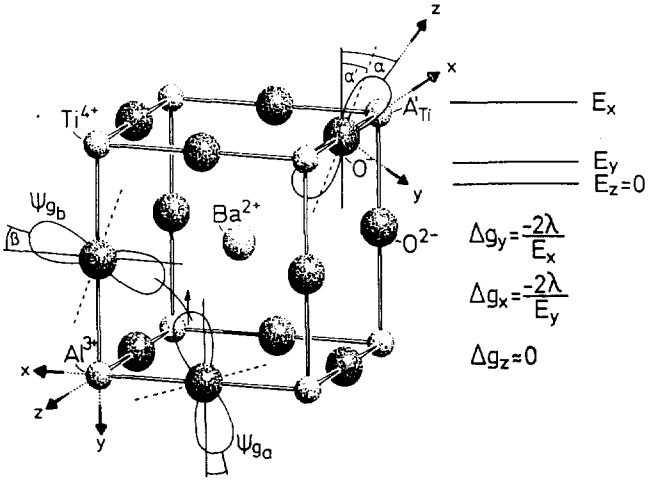

Figure 12. Models of the orbital structure of O^- trapped hole centres in $BaTiO_3$. Upper right: model of O_c^- (see table 3). The level scheme on the right is shown to explain the sequence of the observed g-shifts. Lower left: orbital structure of O^-–Al^{3+}.

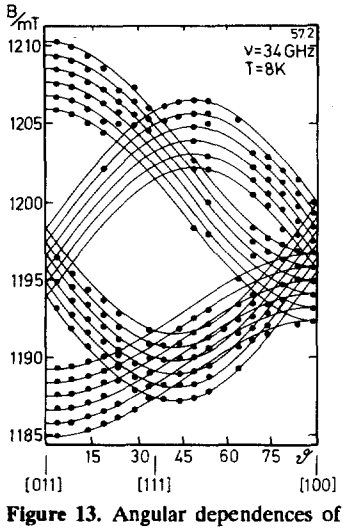

Figure 13. Angular dependences of the resonances of O^-–Al^{3+}.

nodal planes of the groundstate O^- orbital, Ψ_g. This means that Ψ_g is an O^- p–π-type orbital or a linear combination of such orbitals. The principal direction 2 of the orthorhombic g-tensor is aligned along a [100] type direction. So Ψ_g must be of such a nature that the g-tensor has (100) as a mirror plane. Since the other two principal axes of g are extending along the [011] and [01$\bar{1}$] directions, Ψ_g must be a superposition of orbitals of two neighbouring O^- ions in the (100) plane next to Al as shown in figure 12:

$$\Psi_g = N(\Psi_{g_a} - \Psi_{g_b})$$
$$N^{-2} = (2 - 2S) \qquad S : \text{overlap integral.} \tag{6}$$

(The sign chosen in Ψ_g is irrelevant for the following results). For the calculation

of the g-shifts caused by such two-centre wavefunctions it is advisable to use the expression [43]

$$\Delta g_{ij} = -2 \sum_n \frac{\langle \Psi_g | V_{so,i} | \Psi_n \rangle \langle \Psi_n | L_j | \Psi_g \rangle}{E_n - E_g}. \tag{7}$$

Ψ_n are the excited two centre O^- states, and V_{so} is the operator of the spin–orbit coupling: $V_{so} \propto E \times p$, p being the momentum of the unpaired electron and E, the electric field at the electron site. Since E is strong only near the ion cores, the contributions from the overlap regions between both O^{--} ions can be neglected and the problem reduces to an addition of the spin–orbit contributions of the separated ions to Δg [43]

$$\Delta g_{ij} \approx -2\lambda \sum_{n;v=a,b} \frac{\langle \Psi_{g,v} | L_i | \Psi_{n,v} \rangle \langle \Psi_{n,v} | L_j | \Psi_{g,v} \rangle}{E_n - E_g}. \tag{8}$$

Since the overlap contribution to the normalization N remains (equation (6)), this relation holds only approximately. Along none of the principal directions of the g-tensor is a value close to g_e measured; this would be expected if B was parallel to the axis of a p orbital. This indicates that the groundstate p-type orbitals are not aligned along any of these principal directions. We thus conclude that the p orbitals at each of the two O^{--} ions, which compose the groundstate wavefunction, are tilted with respect to the principal axes, as indicated in figure 12. The ground and first excited states at ion a are thus given by

$$\begin{aligned} \Psi_{g,a} &= -\psi_x \sin\beta + \psi_y \cos\beta \\ \Psi_{e_1,a} &= \psi_z \\ \Psi_{e_2,a} &= \psi_x \cos\beta + \psi_y \sin\beta \end{aligned} \tag{9}$$

taking into account that p orbitals transform as vectors. Corresponding expressions hold for ion b. Using these orbitals in equation (8), calculating the matrix elements and summing over the excited states Ψ_{e_1} and Ψ_{e_2} and over ions a and b, one arrives at a Δg-tensor, which contains off-diagonal matrix elements. Diagonalization leads to

$$\begin{aligned} \Delta g_1 &\approx -\frac{2\lambda}{E_{e_1} - E_g}(1 + \sin 2\beta) \\ \Delta g_2 &\approx -\frac{2\lambda}{E_{e_1} - E_g}(1 - \sin 2\beta) \\ \Delta g_3 &\approx -\frac{4\lambda}{E_{e_2} - E_g}. \end{aligned} \tag{10}$$

Coincidence with the measured Δg_i is obtained if $\beta \approx 20°$ is assumed. With $\lambda_{O^-} \approx 150\ cm^{-1}$ [44], $E_{e_1} - E_g \approx 10000\ cm^{-1}$ and $E_{e_2} - E_g \approx 25000\ cm^{-1}$ is predicted. The corresponding optical crystal field transitions are expected to be masked by the small polaron absorptions typical for these O^- centres [45].

The tilting of the orbitals, expressed by these results, is not unexpected: It represents the compromise between the following two influences. The hole groundstate at each O^- site is repelled by the neighbouring Al^{3+} and Ti^{4+} ions, tending to align this ground orbital perpendicular to the Al^{3+}–Ti^{4+} direction. Such π-character is usually found for O^- centres in oxide perovskites [42,46]. The formation of the bond between the two O^- ions contributing to the groundstate tends to tilt the component orbitals away from the pure π-orientation toward maximal overlap.

5. Discussion

It has been shown that ESR studies can identify a large number of various paramagnetic lattice perturbations in $BaTiO_3$. The method thus can serve as a tool for quality control, establish a basis for investigations of the defect chemistry in real $BaTiO_3$ and help to elucidate the role of these defects in photorefractive phenomena in this material.

We have seen that even in nominally undoped material in general many such defects exist, and there are great differences between specimens obtained from different sources with respect to defect types as well as their charge states and their concentrations. ESR can assist in selecting those crystals best suited for photorefractive applications or to help in finding the most effective defects. It should be taken into account, however, that the investigated crystals certainly always contain a number of defects which are ESR silent, because they have diamagnetic groundstates or spin–lattice relaxation times which are too short. Table 1 includes such defects. Their presence was established indirectly by interpreting the light-induced charge changes, to be described in II, in a consistent way. The combination of ESR studies with simultaneous optical absorption measurements is in preparation. In this way we hope to identify also ESR silent defects directly and to arrive, eventually, at a more complete overview on the defect scenario in a given $BaTiO_3$ specimen.

Compensation of charged defects in real undoped $BaTiO_3$, as investigated here, certainly is more involved than the mechanisms proposed for ideal material, where a smaller number of defect types is generally assumed. Still in all crystals studied there is a preponderance of acceptor defects (see table 1), such as Fe^{3+}, the centre with the highest concentration in almost all crystals.

This is in accord with the fact [47] that the defect scenario in $BaTiO_3$ is dominated by acceptors, A', compensated by oxygen vacancies, $V_O^{\cdot\cdot}$, containing no electrons. By annealing in an oxygen rich atmosphere, $V_O^{\cdot\cdot}$ are expected [47] to be replaced by oxygen ions, neutral with respect to the lattice. The resulting holes are then captured at low temperatures at the acceptor ions, A', forming neutral A^x, or being excited to the valence band, leading to hole conduction at elevated temperatures. It will be interesting to observe, in future redox studies, whether this behaviour can be found with ESR. It should be noted that also donor defects have been observed in the groundstate of the crystals (table 1), partly but not totally compensating the acceptor charges. Shell model calculations [48] of defects in $BaTiO_3$ support the above experimentally derived views on the behaviour of defects in $BaTiO_3$.

Both types of studies also emphasize that the solubility of TiO_2 in $BaTiO_3$ is rather low. The concentration of Ba vacancies, V_{Ba}, was found to be below 100 ppm. Also the presence of V_{Ti} is rather unlikely, because its formation needs a rather high energy, 4.25 eV [48].

As will be shown in II, one can draw important conclusions on the contributions of the detected lattice perturbations to light-induced charge transfer processes. Special results have been listed in the introduction and will be further elaborated in II. Here we limit ourselves to general remarks. Already the fact that charge changes can be observed in $BaTiO_3$ by ESR is in contrast to the situation in, e.g., $LiNbO_3$ doped with Fe. Here the phototransport is described by a '1-centre model': by inhomogeneous illumination Fe^{2+} is photoionized and the quasifree electron is trapped at Fe^{3+} in the dark regions, again forming Fe^{2+}. So there is no net change of the Fe^{2+} and Fe^{3+} concentrations and the ESR spectra are not altered. On the other hand, charge

conversions of defects in $BaTiO_3$ are observed with ESR at low temperatures. So at least two types of centres must be involved in light-induced charge transport in $BaTiO_3$: charge carriers photoionized from one defect-type are captured at another one, leading to the observed ESR changes. Measurements of the dependence of photoconductivity on light intensity further require that one of the centres is connected with shallow levels, the other defect with deep ones [3]. This model also applies to charge transport in other oxide perovskites, such as $KNbO_3$; here also light-induced charge changes have been observed in ESR [49].

Acknowledgments

We thank Dr J Albers, Professor G Godefroy, Dr H Hesse and Dr D Rytz for generously making available the crystal specimens used in the present investigation. The experimental support by T Dollinger and W Koslowski is gratefully acknowledged. This work was performed within Sonderforschungsbereich 225 'Oxide crystals for electro-optical and magneto-optical applications', supported by DFG.

References

[1] Klein M B 1988 *Photorefractive materials and their applications (Springer Topics in Applied Physics 61)* ed P Günter and J P Huignard (Berlin: Springer) pp 195–236
[2] Brost G A, Motes R A and Rotge J R 1988 *J. Opt. Soc. Am.* B **5** 1879
[3] Holtmann L 1989 *Phys. Status Solidi* a **113** K89
[4] Mahgerefteh D and Feinberg J 1990 *Phys. Rev. Lett.* **64** 2195
[5] Holtmann L, Groll A, Unland M, Krätzig E, Maillard M and Godefroy G 1990 *Topical Meeting on Photorefractive Materials, Effects and Devices II (Aussois, France)* pp 83–6
[6] Müller K A 1981 *J. Physique* **42** 551
[7] Müller K A, Berlinger W, Blazey K W and Albers J 1987 *Solid State Commun.* **61** 21
[8] Müller K A, Berlinger W and Albers J 1985 *Phys. Rev.* B **32** 5837
[9] Schwartz R N, Wechsler B A and Rytz D 1990 *J. Am. Ceram. Soc.* **73** 3200
[10] Possenriede E, Schirmer O F, Albers J and Godefroy G 1990 *Ferroelectrics* **107** 313
[11] See, e.g., Abragam A and Bleaney B 1970 *Electron Paramagnetic Resonance of Transition Ions* (Oxford: Clarendon)
[12] Sakudo T and Unoki H 1964 *J. Phys. Soc. Japan* **19** 2109
[13] Possenriede E, Schirmer O F, Donnerberg H J, Godefroy G and Maillard A 1989 *Ferroelectrics* **92** 245
[14] Auzins P V and Wertz J E 1967 *J. Phys. Chem.* **71** 211
[15] Schirmer O F, Berlinger W and Müller K A 1975 *Solid State Commun.* **16** 1289
[16] Low W 1958 *Phys. Rev.* **109** 256
[17] Žďánský K, Arend H and Kubec F 1967 *Phys. Status Solidi* **20** 653
[18] Abragam A and Pryce M H L 1951 *Proc. R. Soc.* A **206** 173
[19] Possenriede E, Schirmer O F, Donnerberg H J and Hellermann B 1989 *J. Phys: Condens. Matter* **1** 7267
[20] Aguilar M 1984 *Solid State Commun.* **50** 839
[21] Possenriede E, Gerlich F and Schirmer O F to be published
[22] Kirkpatrick E S, Müller K A and Rubins R S 1964 *Phys. Rev.* **135** A86
[23] Blazey K W, Müller K A, Berlinger W, Cabrera J M and Aguilar M 1984 *XXIInd Congress Ampere on Magnetic Resonance and Related Phenomena (Zürich, Switzerland)* pp 182–3
Blazey K W, private communication
[24] Šroubek Z, Žďánský K and Šimánek E 1963 *Phys. Status Solidi* **3** K1
[25] Šimánek E, Šroubek Z, Žďánský K, Kaczér J and Novák L 1966 *Phys. Status Solidi* **14** 333
[26] Bukhan'ko F N and Bratashevskii Y A 1975 *Ukr. Fiz. Zh.* **20** 680
[27] Bukhan'ko F N 1980 *Sov. Phys.–Solid State* **22** 1174

[28] Bukhan'ko F N and Bratashevskii Y A 1981 *Sov. Phys.–Solid State* **23** 456
[29] Williams F I B, Krupka D C and Breen D P 1969 *Phys. Rev.* **179** 255
[30] Ham F S 1972 *Electron Paramagnetic Resonance* ed S Geschwind (New York: Plenum)
[31] Raizman A, Suss J T and Szapiro S 1970 *Phys. Lett.* **32A** 30
[32] Suss J T, Low W and Foguel M 1970 *Phys. Lett.* **33A** 14
[33] Thornley J H M 1968 *J. Phys. C: Solid State Phys.* **1** 1024
[34] Schirmer O F, Förster A, Hesse H, Wöhlecke M and Kapphan S 1984 *J. Phys. C: Solid State Phys.* **17** 1984
[35] Possenriede E, Schirmer O F and Godefroy G 1990 *Phys. Status Solidi* b **161** K55
[36] Lagendijk A, Morel R J, Glasbeek M and van Voorst J D W 1972 *Chem. Phys. Lett.* **12** 518
[37] de Jong H J and Glasbeek M 1978 *Solid State Commun.* **28** 683
[38] See, e.g., Juppe S and Schirmer O F 1986 *Phys. Lett.* **117A** 150
[39] Takeda T and Watanabe A 1966 *J. Phys. Soc. Japan* **21** 267
[40] Müller K A, Berlinger W and Rubins R S 1969 *Phys. Rev.* **186** 361
[41] See, e.g., Henderson B and Wertz J E 1977 *Defects in the Alkaline Earth Oxides* (London: Taylor and Francis)
[42] Schirmer O F, Berlinger W and Müller K A 1976 *Solid State Commun.* **18** 1505
[43] Slichter C P 1990 *Principles of Magnetic Resonance* (Berlin: Springer)
[44] Schirmer O F 1978 *J. Phys. C: Solid State Phys.* **11** L65
[45] Schirmer O F 1976 *Z. Phys.* B **24** 235
[46] Possenriede E, Hellermann B and Schirmer O F 1988 *Solid State Commun.* **65** 31
[47] Smyth D M 1984 *Prog. Solid State Chem.* **15** 145
[48] Lewis G V and Catlow C R A 1986 *J. Phys. Chem. Solids.* **47** 89
[49] Jacobs P, Possenriede E and Schirmer O F 1992 *to be published*